Aerodynamic Control of a Cylindrical Platform at High Angles of Attack using Forebody Bleed

Edward Lee [1], Bojan Vukasinovic[2], and Ari Glezer[3]
Woodruff School of Mechanical Engineering,
Georgia Institute of Technology, Atlanta, GA 30332-0405

Abstract

Dynamically-controlled aerodynamic bleed across the segmented surface of the forebody of a cylinder platform model at high angles of incidence ($30^o < \alpha < 60^o$) is explored for manipulation of the aerodynamic side forces and can either null or effect a desired side load. It is shown that localized interaction of the bleed with the flow near the forebody's front stagnation point forces flow symmetry about the cylinder and a nearly balanced resultant side force, while bleed interactions with the formation of each forebody vortex results in its premature displacement away from the cylinder while the other vortex remains in close proximity to surface and bends towards the axis of symmetry. Switching the bleed actuation about the azimuthal point of symmetry can lead to rapid variations in the side force coefficient between $C_s \approx$ -3.5 to 3.5 within azimuthal bleed orientations of ±15°. It is shown that the evolution of the forebody vortex pair trajectories and their circulations are good indicators of the magnitude and direction of the resultant side force. The present results indicate that typical random side load on an axisymmetric body at high angles of incidence can be overcome by controllable azimuthal aerodynamic bleed.

I. Background

A number of studies have considered the flow around axisymmetric bodies with streamlined forebodies at high angles of attack, including missiles, rockets, and fighter aircraft. The behavior of aerodynamic flow and forces around such cylindrical bodies are predominantly influenced by a series of vortical structures that commence with a pair of counter-rotating forebody vortices and progresses through successive interactions with the shear layers bounding the near wake on the leeward side of the cylindrical body.

Earlier investigations have emphasized the critical role of the change in symmetry in the evolution of forebody vortices as the angle of attack increases. Studies by Ericsson and Reding (1986) and Zilliac et al. (1991) pointed out the critical transition to asymmetrical vortex pair evolution with the pitch angle increase, depending on the forebody tip angle and orientation. This asymmetry is precipitated by premature detachment of one forebody vortex, inducing the undesirable side forces and yawing moments with the downstream asymmetric propagation, as discussed by Allen and

[1] Graduate Research Assistant, AIAA Member.
[2] Research Engineer, AIAA Member.
[3] Professor, AIAA Fellow.

Perkins (1951). Furthermore, this lateral load-inducing phenomenon at high angles of attack is not limited only to axisymmetric bodies. Del Frate and Saltzman (1992) presented the flow visualization of X-29 fighter jet forebody as the resulting unbalanced side force was detected on the aircraft. Also, Nelson and Pelletier (2003) showed the development of asymmetric vortical structure about the forebody and leading edge for aircraft with slender forebody and a sharp-edge delta wing, respectively. Subsequent investigations focused on identifying the sources of this aerodynamic behavior. Keener and Chapman (1974) confirmed a dependency of forebody vortex asymmetry evolution on forebody geometry, while a number of studies emphasized the sensitivity of the vortex pair evolution to minor surface imperfections (e.g., Thomson and Morrison 1971, Chapman et al. 1976, Yanta and Wardlaw 1977 and 1981, Lamont 1982). More recently, Mahadevan et al., (2018) showed that even the highly treated and polished axisymmetric forebodies still exhibit the vortex pair, and thereby the induced side forces sensitivity, to the forebody azimuthal orientation. In addition, a numerical study by DeSpirito (2017) pointed out the presence in asymmetry even in the spin-stabilized axisymmetric bodies at high angles of attack.

These previous investigations regarding the high sensitivity of forebody vortex evolution to surface perturbations also suggest a potential avenue for controlling aerodynamic loads at high angles of attack with relatively weak control input. Hence, both passive and active forebody flow control techniques have emerged over years to manipulate forebody vortex evolution, primarily aimed at mitigating the undesired side forces and yawing moments caused by asymmetric vortex-wake coupling. Earlier work by Ericsson and Reding (1980) assessed the impact of trip wires on the forebody to alleviate vortex-induced side loads, while Xueying et al. (2002) explored passive methods by introducing spherical and rectangular perturbations near the forebody tip to influence the bi-stable realization of forebody vortices. In an extension of passive surface modifications, Leu et al. (2005) experimented with an array of inflatable micro-balloon actuators mounted on a conical forebody's surface to induce the formation of asymmetric vortices, thus inducing side forces in a desired direction. Beyond passive means, studies on active flow control involving jet actuation at or near the forebody tip have also been pursued. Kumar et al. (2008) showed that a control jet issuing through the tip and into the oncoming flow can induce ‘fluidic blunting’ of the tip, alleviating the net side force. Porter et al. (2014) illustrated the side force response through open and closed-loop control of the blowing port or starboard actuator at the forebody tip. Additionally, Wang et al. (2018) demonstrated the use of a dual synthetic jet actuator installed upstream on the ogive forebody to modify the distribution of forebody vortices by employing different jet duty cycles. Besides the direct forebody vortex pair control over their initial domain, indirect control approach was proposed by Lee et al. (2021a), utilizing a synthetic jet to control the near wake at the forebody juncture, indirectly affecting the forebody vortex pair evolution and subsequently altering resulting net side forces. In a companion investigation (Lee et al., 2021b), this indirect control of forebody vortex evolution was extended to suppress instabilities of the axisymmetric model within a narrow range of high angles of attack that triggered the model unstable response.

Another approach that was shown to suppress side force loads on axisymmetric body at high incidence involved increasingly perforated extent of the forebody, extending into the cylindrical body and thereby utilizing the aerodynamic bleed driven by pressure differences to enforce flow symmetry (Bauer and Hemsch, 1994). They showed that the increase in incidence of the onset of a nonzero side force was proportional to the axial extent of the bleed. Similarly, Fears (1995) presented comparable outcomes while examining an alternative method to using strakes for

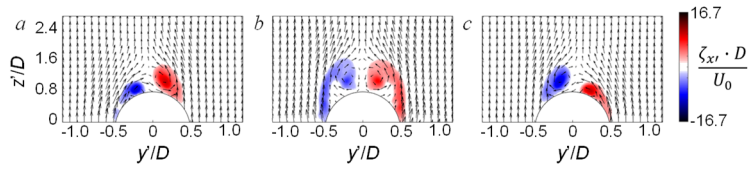

Figure 1. *Color raster plots of time-averaged, body-streamwise vorticity $\zeta_{x'}$ overlaid with velocity vectors at $x'/D = 1.6$ for the segmented, top-right side (a), the full circumferential (b), and top-left side (c) forebody bleed.*

generation of yawing moments, by replacing the solid forebody of a fighter aircraft model with a porous forebody. The present investigation is motivated by the earlier work of Lee et al. (2023), who demonstrated that segmented porosity over the forebody of a cylindrical platform can alter the naturally-evolving aerodynamic loads at high angles of attack. To illustrate the three characteristic flow topologies induced by the segmented aerodynamic bleed, Figure 1 shows color raster plots of the mean streamwise vorticity overlaid with subsets of velocity vectors at $x'/D = 1.6$, downstream from the forebody. The differences between the evolution of the flow fields past the different configurations of the forebody bleed segments indicate that this flow control approach is capable of not only suppression of a nonzero side force but can also induce controlled flow asymmetries and thereby a desired side force. The vortex/flow asymmetry is clearly introduced by the premature vortex displacement on the bleed forebody quadrant side in Figures 1a and c, while the full azimuthal bleed (Figure 1b) prematurely but symmetrically displaces both forebody vortices away from the surface. Consequently, the vortex-wake coupling under the asymmetric bleed configurations is further considered for bi-directional aerodynamic control in the present investigation, while the enforcing vortex-wake symmetry of the symmetric bleed interactions is explored for suppression of the natural asymmetric aerodynamic side loads.

II. Experimental Setup and Procedures

The experimental investigation utilizes a slender axisymmetric model of a cylindrical body (diameter $D = 50$ mm, length $L = 9D$) with a tangent $2D$-long ogive forebody analogous to that of the prior study by Lee et al. (2023). The present investigations focus on superseding the naturally-evolving aerodynamic loads that form autonomously over a range of angles of incidence ($30° < \alpha < 60°$) at cross stream speeds of up to $U_\infty = 26$ m/s ($Re_D = 8.6 \cdot 10^4$) by dynamically-controlled aerodynamic bleed over the forebody.

The axisymmetric model is wire-supported in an open-return wind tunnel (test section measuring 91 cm on the side) by a dynamic 6-DOF eight-wire traversing mechanism (Figure 2a) described in detail by Lambert et al. (2016). Each support wire has an in-line load cell and is controlled by an independent servo motor. The forces and moments on the model are calculated from the measured wire tensions projected onto the model (the resultant aerodynamic loads on the model are calculated relative to the loads in the absence of cross flow, and accounting for wire drag). The attitude of the model is commanded by a *MATLAB Simulink* controller, which feedback utilizes inputs from *VICON* motion-capture camera system at an update rate of 500 Hz. Besides providing the feedback signal, the six-camera motion capture system resolves the spatial and temporal position of the model at any instant in time. In an alternate configuration, the feedback loop can be disconnected with the servo motor brakes enabled to 'lock' the model in the desired attitude to emulate a limited 'free-flight' condition. Either configuration is utilized, depending on the desired body constraints. The information regarding the model position/orientation is used to extract the wire orientation and accurately decompose the forces measured on each load cell into x, y, and z components in real time. In addition to the measurement of the aerodynamic loads, a planar PIV

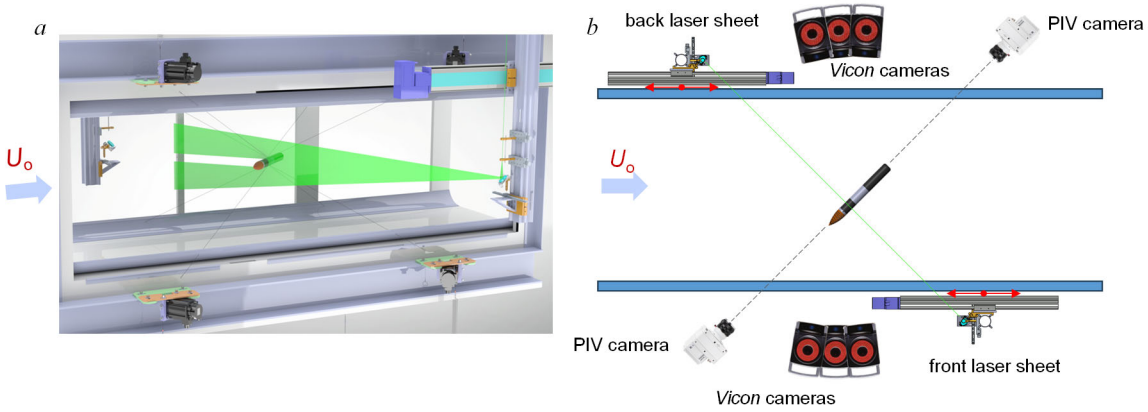

Figure 2. *CAD model of the leeward PIV illumination (a) and schematics of the dual PIV setup (b).*

system is used to characterize the model's forebody vortices and the wake using a CCD camera aligned with the axis (*x*' in Figure 3) of the model, imaging 532nm Nd:YAG laser sheet such that the measurement plane is normal to the model's axis, as illustrated schematically in Figure 2a. A detailed PIV characterization of the flow about the slender axisymmetric body at high angles of attack is designed such that the measurements can be done over both the windward and leeward sides of the body's cross-section. For that purpose, the laser-sheet optical paths were assembled on either side of the wind tunnel test section, as shown schematically in Figure 2b. Laser beam is initially directed to a linear traverse on the top of the test section carrying two 45° mirrors, where one mirror directs the beam to the front and the other to the back of the test section. Both sides of the wind tunnel have identical optical paths that direct the beam to the next mirror atop the vertical rail attached to the computer-controlled traverse. After being directed downward and passing through spherical and cylindrical lenses, the laser sheet is finally directed horizontally intersecting the model's cross section and illuminating either the windward (not shown) or leeward (Figure 2a) side of the flow about the model. Each PIV camera is mounted on its own linear traverse, aligned with the model axis (Figure 2b). All the PIV measurements are done by the following procedure. The PIV camera is positioned at the starting distance from the model, at the focal length of the first measurement plane. Then, the laser beam is steered to the front forming the illuminated sheet on the vortex pair / leeward side. Once the PIV measurements are taken on this side, the laser beam is then steered to the back by the second mirror on the top and the complementary PIV measurements are taken on the windward side of the model. Once such a pair of the PIV measurements is completed, both the laser sheet (still directed from the back) and the PIV camera are axially (x'-direction) incremented to the next measurement plane, and the next pair of PIV measurements are taken over the windward and leeward sides. This advancement in the axial direction is subsequently repeated over all the measurement planes. In the present investigation, focus is placed on the interaction domain between the oncoming flow and the bleed control, resulting in the 34 dual-measurement planes between $x'/D = 0.1 - 3.4$.

III. Evolution of the Forebody Vortex Pair in the Base Flow

The present work particularly focuses on the control-induced aerodynamic states of the body at high angles of attack, regardless of what such states would be realized in the absence of control. Particularly, this is motivated by an apparent random orientation of the naturally-evolving vortex/flow asymmetry, which was documented in literature (e.g., Hunt 1982, Porter et al. 2012, and Mahadevan et al. 2018) and in the prior work by Lee et al. (2021a, 2021b). Hence, the present work

focuses on the tailored realization of bi-directional aerodynamic load realizations for introducing the flow asymmetries of preferred orientation, including the enforced symmetry that results in suppression of the side loads.

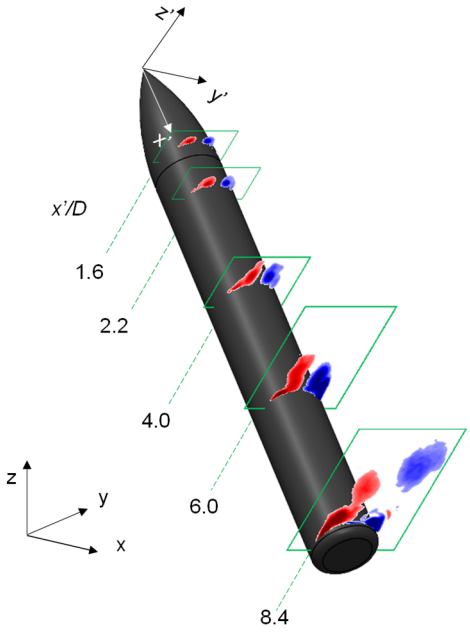

Figure 3. *Five PIV planes showing color raster plots of body-streamwise vorticity $\zeta_{x'}$ in the base flow over the axisymmetric body.*

To illustrate the base flow over the model in the absence of the bleed control, the color raster plots of the streamwise vorticity relative to the body coordinate system (x') at five cross stream planes along the model are shown in Figure 3 for the pitch angle α = 50° (Lee et al., 2023). The initial formation of the forebody vortex pair at x'/D = 1.6 is reasonably symmetric and vortices have nearly identical magnitudes of vorticity (and its integral measure of circulation). The symmetry appears to be still preserved at x'/D = 2.2, where only the entrainment-driven growth of the vortices is measured. Some disruption in symmetry is noted at x'/D = 4, where both vortices begin to deflect away from the surface. By x'/D = 6, the two forebody vortices appear to have been grown away from the surface without detachment, while the CW and CCW vortex sheets on both sides of the body's surface begin to roll up underneath the primary vortex pair. The asymmetry in the shedding of the forebody vortices downstream from x'/D = 6, as is evidenced by their trajectories, is also manifested by an induced net negative side force (along $y' < 0$) as a result of the local wake asymmetry introduced by earlier displacement of the CW vortex and the prolonged azimuthal flow attachment on the CCW vortex side. The topology of the streamwise vorticity at x'/D = 8.4 indicates that the asymmetry propagates downstream, as the CW vortex is seen displaced further into the wake than its corresponding CCW pair. Furthermore, formation of the secondary vortex pair about the cylindrical body continues underneath the displaced primary vortex pair, and their asymmetry further contributes to the net side force. While the evolution of the base flow about the model indicates a natural forming asymmetry that favors a net negative side force on the model, it should be emphasized that minor rotations of the forebody orientation relative to the oncoming flow can and do trigger a different asymmetry in the vortical/wake evolution about the body, favoring a net resultant side force of the opposite sense. Lastly, once the angles of attack become sufficiently high (depending on the forebody conical angle), the flow coupling to the body always become asymmetric with a finite resultant side force.

IV. Bleed-induced Flow States and Aerodynamic Loads

As noted in §II, the distribution of the forebody bleed ports in the present investigations is similar to the bleed model that was used by Lee et al. (2023). The bleed pattern consists of and axial distribution of twenty azimuthal bleed port arrays each with seven rectangular streamwise-orientated ports as shown in Figure 4b, amounting to overall 20% porosity over the forebody. However, the bleed forebody in the present investigation consists of outer and the inner shells (Figure 4a), where the inner shell is utilized as a "valve" that regulates which segments of the bleed ports of the outer shell are open. Furthermore, an active bleed control device is devised that can

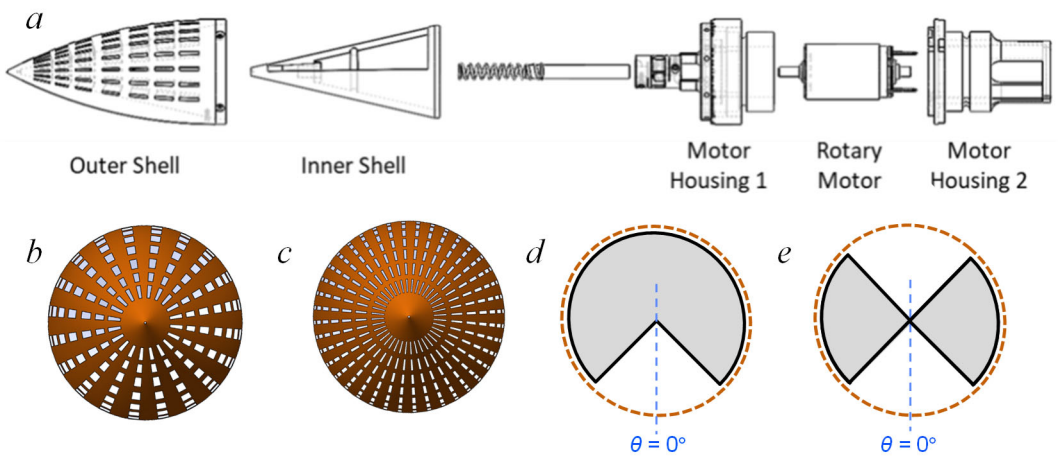

Figure 4. *Forebody bleed control module driven by a rotary motor (a), the default (b) and dense (c) forebody bleed shell models with 20% porosity, and a single- (d) and dual-path (e) inner shell designs.*

be controlled remotely and tailor the bleed control in real time. For that purpose, a miniature rotary motor with encoder feedback is integrated into the model (Figure 4a), having an azimuthal step resolution of 0.176°. The motor shaft is extended such to connects to the inner shell - an internal conical segment with partition azimuthal opening that is inserted in the forebody, and it is positioned under the outer shell which is populated with arrays of bleed ports. In addition to the outer shell having the bleed port distribution identical to the prior study (Figure 4b, Lee et al., 2023), another finer bleed pattern (Figure 4c) is tested, both having the total porosity of 20% but the second pattern doubling the number of rows, with the corresponding halving of the total bleed path per row. In addition, while the default inner shell configuration is designed after the results of the initial investigation (Lee et al., 2023), having a conical azimuthal opening of 90°, as illustrated in the schematics in Figure 4d, another inner shell configuration, providing a directional bleed path from the high- to the low-pressure side (Figure 4e) is considered as well. As another noteworthy difference relative to the earlier work is that in the present forebody design there is no fully closed configuration (zero bleed) and there is always an azimuthal 90° segment of the that surface that is open for bleed, depending on the orientation of the inner shell. As already noted above, the main objective of the present investigations is to demonstrate that bleed actuation can directly control the body aerodynamics and thereby bypass any flow state that might exist in the absence of the actuation.

The initial assessment of the bleed effect on the aerodynamic loads on the cylinder was done relative to the center azimuthal orientation of the inner-shell $\theta = 0$ which defines the active section of the bleed that spans between $\theta = -45°$ and +45°, as shown schematically in Figure 4d, for a single-path inner shell, or, in the case of a dual-path inner shell (Figure 4e), an additional opposite azimuthal segment is also open between $\theta = +135°$ and +225°. Typical changes in the aerodynamic loads in the fixed coordinate system drag, lift, and side force direction, C_D, C_L, and C_S, respectively, are shown in Figure 5 for four combinations of the forebodies and inner shells. In each set of experiments, the model is kept at the pitch angle $\alpha = 45°$ and the inner shell is initially positioned at $\theta = 0°$, i.e., at the central windward side (z') direction. After a set of the force measurements is taken, the inner shell orientation is incremented in θ and the next set of measurements is acquired. This process is repeated until the inner shell central reference point θ traverses full 360°. These resulting full azimuthal changes in the aerodynamic loads are shown in

Figure 5. Clearly, the dominant change in each case is measured in the side force magnitude and sign due to the primary alteration of the vertical symmetry of the wake due to the bleed control. It should be noted, though, that both drag and lift forces also exhibit smaller pseudo-periodic variation, albeit at much smaller magnitude variation. While the net induced aerodynamic force is not exclusively in the side force direction, the main focus of the subsequent analysis is focused on the side force effects. Another important feature to note is that the peak levels of the induced side force coefficient approach the magnitude of the lift force coefficient in any configuration shown in Figure 5. When assessing the differences between the default and dense bleed distributions, for a single path inner shell (Figures 5a and c), there are more azimuthal variations for the dense distribution, although, in principle, aerodynamic behavior is quite similar. The side force switches sign/direction about two azimuthal orientations close to $\theta = 0°$ and 180°, while over the range of angles up to 180° and past 180° remains of the same sign, with some variations in magnitude. It is argued that the characteristic locations θ for the flow asymmetry / force switch are located underneath of the forming vortex pair on the leeward side ($\theta \approx 180°$) and their associated stagnation point, and underneath the windward side stagnation point ($\theta = 0°$), as these two regions of the flow are the most susceptible to perturbations. Interestingly, the periodicity in the side force coefficient cycle doubles for the dual-path inner shell (Figures 5b and d). In addition to the two critical azimuthal orientations for the single-path inner shell, the dual-path inner shell introduces another pair of critical points about the inner shell horizontal orientation. It can be expected that the nominal flow symmetry would be established for the dual-path horizontal orientation when, ideally, there would be no pressure difference across the inner shell. The zero-crossing of the side force at approximately $\theta \approx 0°$, 90°, 180°, and 270° implies the force maxima/minima to form in between these four critical orientations, which is clearly seen in Figures 5b and d. The primary modification of the force response in the dense bleed path (Figure 5d) is expressed through the extended leveling about the peak positive and negative magnitudes relative to the default bleed pattern. After these initial assessments, the remaining investigation is focused on the single-path bleed through the default bleed-pattern forebody shell (cf. Figure 4b and d).

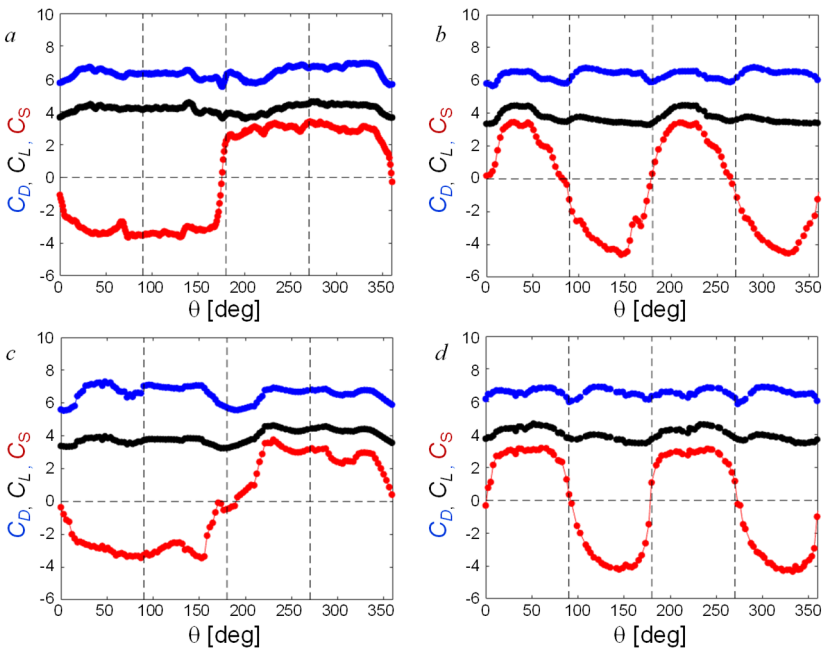

Figure 5. *Drag (C_D), lift (C_L), and side (C_S) force coefficients for the default (a,b) and dense bleed (c,d) forebodies and a single- (a,c) and dual-path (b,d) inner shells with respect to the shell azimuthal orientation θ (α = 45°, U_o = 26 m/s).*

From the standpoint of flow control, another important parameter aside from the azimuthal points about which the force changes sign/direction, is the rate of change of the force coefficient with

angular displacement $dC_s/d\theta$, governing the sensitivity of the controlled parameter to the control input change, in this case the angular orientation of the single-path bleed inner shell, θ. Regarding this slope, it is clear from the plots in Figure 5 that, typically, the rising slope is higher than the falling slope, facilitating the full-magnitude force switch over ±12-15° about the critical point (zero force). Still, within these bounds, the higher slope on the rising side makes this critical point a better candidate for the flow control when the fastest response is sought, while the falling slope would be preferred when finer resolution in the force adjustment is of the primary interest. In order to gain a better understanding of this $dC_s/d\theta$ sensitivity across angles of attack, the full C_s-θ sweeps of Figure 5 (α = 45°) are repeated for 30° ≤ α ≤ 60°, with an increment of 2.5°. The extracted rising and falling slopes are shown in Figure 6 over the full range of the pitch angles. In principle, the main conclusions of the analysis of the single sweep of Figure 5a hold for any tested angle since the rising slope remains higher throughout the pitch angle sweep. It is interesting, though, that both the rising and falling slopes do not change significantly over the lower pitch angles for which the naturally flow over the axisymmetric model tends to remain symmetric in the absence of control, below $\alpha \approx 40°$. As the pitch angle increases further, notable excursions are recorded, implying increased sensitivity as the natural flow develops into asymmetric flow topology. Therefore, it is not surprising that the highest control sensitivity is measured about the highest angles of attack, both along the rising and falling slopes. As a tradeoff for the increasing sensitivity, it should be noted that balancing a zero net side force becomes progressively more challenging as the sensitivity of the flow drives it naturally to either asymmetric state for even the smallest angular displacements of the inner shell. It is likely that any specific control solely interested in maintaining a zero, or near-zero, side force may consider adjustments in the bleed shell configurations to readjusts the slopes of $dC_s/d\theta$ to lower levels, more comparable to those of the lower range of the angles of attack.

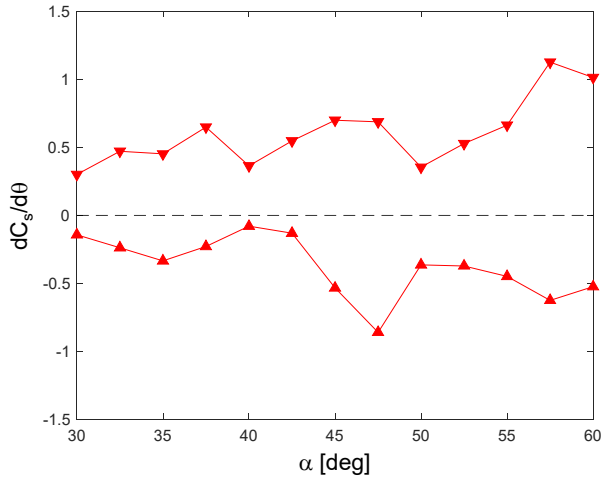

Figure 6. *Change of the side force coefficient slope with the bleed inner shell orientation over the rising (▼) and falling (▲) C_s – θ transitions (cf. Figure 5a) across the full range the angles of attack for U_o = 26 m/s.*

An example of the bi-directional control range about the windward stagnation point on the body is shown in Figure 7 for the single-path inner shell over the default forebody bleed. First, as noted earlier, zero-crossing on the windward side, around which bi-directional control is centered, is not located exactly along the vertical symmetry plane but rather at about θ = -2.5° in the present case. This is attributed to the naturally biased flow symmetry (in the absence of flow control) and it can be argued that, to restore symmetry, control has to offset such a natural state. Schematic representation of the suppressed side force is shown in Figure 7c, indicating the resultant force coefficient of about $C_s \approx 0.13$. In addition, it is outlined how the control inner shell excursions of only ±15° from this point are sufficient to switch the resultant force coefficient between $C_s \approx 0.13$ (Figure 7b) and -2.47 (Figure 7d). These corresponding bounds of the control inner shell range are also marked by the dashed green lines in Figure 7a. Clearly, a similar range of operation can

be deduced across the rising slope of the C_S response in Figure 7a, in which case the bleed control would be effected over the leeward side, along the vortex pair trajectory.

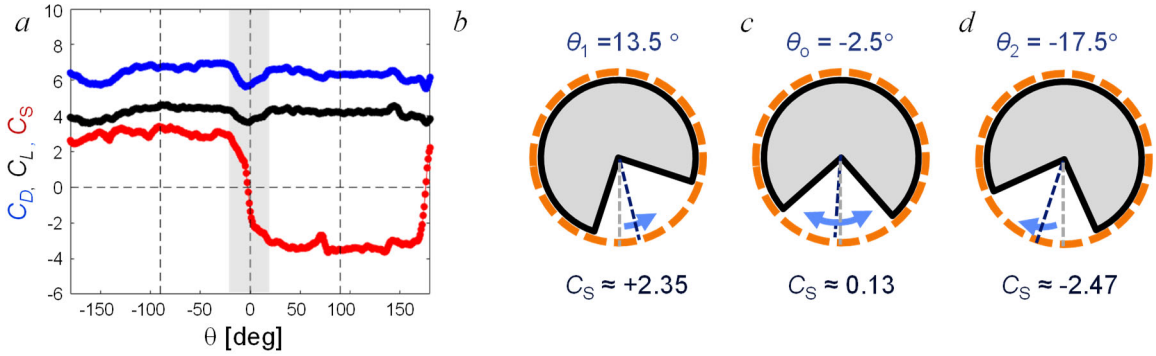

Figure 7. *Azimuthal range of operation of a single-path inner shell for $\alpha = 45°$ and $U_o = 26$ m/s (a) and schematics of the three angular orientations resulting in $C_S = 2.35$ (b), 0.13 (c) and -2.47 (d).*

Another important parameter for flow control application is the flow latency in response to a change in the control input, expressed through the altered aerodynamic loads. As shown in Figure 5, the dominant change is in the side force, although both drag and lift follow such changes at smaller excursions. Hence, the following test of the force response is focused on the side force response. Based on the operational range shown in Figure 7, the single-path inner shell is commanded to periodically switch between the two end states, i.e., between $\theta = -17.5°$ and 13.5°. The inner shell motion is finely adjusted to achieve square-wave transitions and the measured inner shell trajectories are shown in blue in the lower plots of Figure 8. Detailed inspection of the inner shell repositioning between its end states yields the actual time of about 25 ms, regardless of the oscillation frequency. In relation to the flow convective time scale for the flow to traverse the model planform area, this time duration is just under $2.1T_{conv}$. Although the force begins to respond virtually instantly to the inner shell motion (traces in red in the upper row of figure 8), the full establishment of the end state force occurs about 50 ms past the inner shell reaches its end state, or, in convective time scale, that lag is of about $4.2T_{conv}$. Since this lag is nearly invariant within the tested frequency range $f = 0.5 – 6$ Hz, it can be extrapolated that the full switch from positive to negative force (and in reverse) could be rapidly varied beyond 6 Hz, which is in accord with the recorded force change at $f = 6$ Hz (Figure 8d), for which the force rise up to the local maxima/minima is immediately followed by the drop/rise. It is also noted that a dual-path inner shell configuration (cf. Figure 4e) is expected to further reduce this latency in the force response to the bleed control, as the bleed in the single-path inner shell design acts locally, while the dual-path enables direct 'communication' across the wake. Another interesting feature that is visible in all the force traces in Figure 8 is that the nearly step-on change in the control parameter introduces

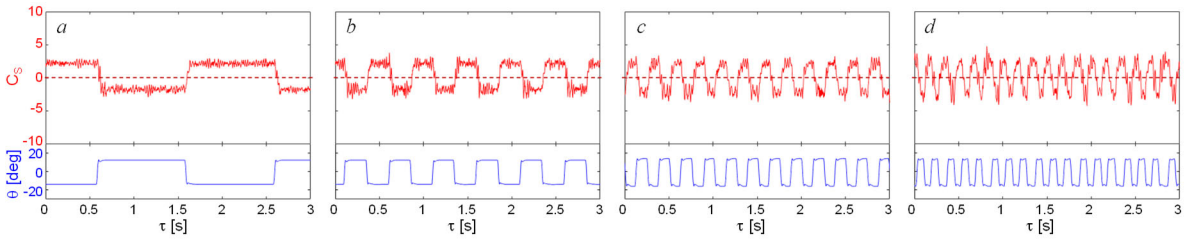

Figure 8. *Bi-directional control of the side force by periodic switching between the $\theta = -17.5°$ and $13.5°$ at $f = 0.5$ (a), 2 (b), 4 (c), and 6 (d) Hz ($\alpha = 45°$, $U_o = 26$ m/s).*

the resonant modulation of the response force signal, which becomes progressively stronger with the switch frequency increase (e.g., compare Figure 8a and d).

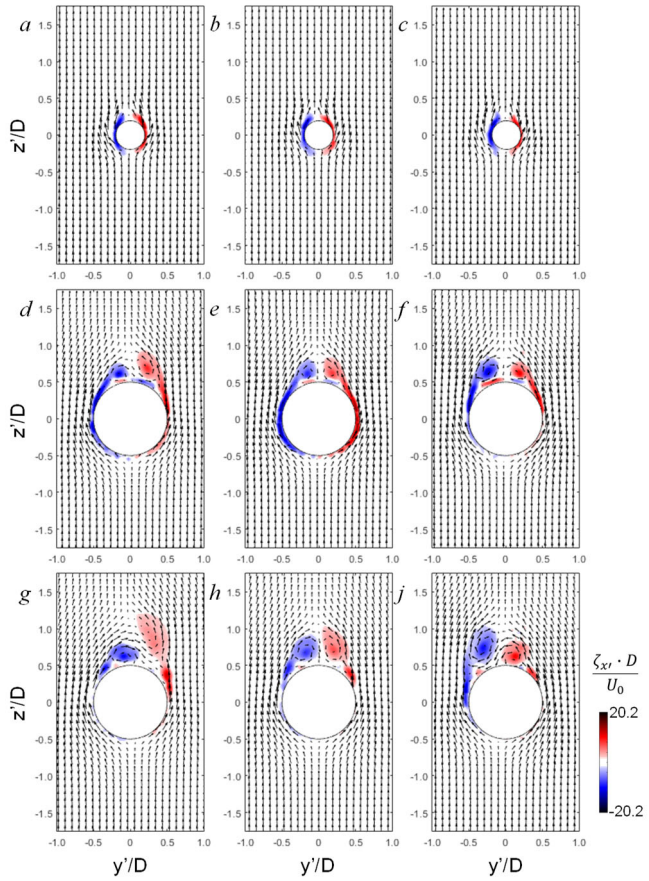

Figure 9. *Color raster plots of time-averaged streamwise vorticity $\zeta_{x'}$ overlaid with every fourth measured velocity vector at x'/D = 0.4 (a–c), 1.8 (d–f), and 2.6 (g–j), for the bleed control centered at θ = 135° (a,d,g), 177° (b,e,h) and 225° (c,f,j); U_o = 26 m/s.*

While the flow field evolution across the full streamwise extension of the axisymmetric model was examined by Lee et al. (2023), the present flow field characterization focuses on the bleed interaction region over the forebody, extended to the upstream cylindrical central body down to x'/D = 3.4. As described in Section II, the dual PIV measurement setup enables measurements of the full flow field about the model. Figure 9 illustrates three characteristic flow fields about the body over the three characteristic flow control outcomes. In addition to the control centered about the windward stagnation point discussed in connection to Figures 7 and 8, the flow fields resulted from the control under the forebody vortex pair are also shown. Therefore, the three control inner shell orientations are θ= 135°, 177°, and 225°, yielding the net side force coefficients C_s = 3.1, 0.2, and -3.3, respectively. Each flow field is shown in terms of raster color plots of the body-streamwise vorticity component $\zeta_{x'}$, with a subset of the mean in-plane velocity vectors, where only every fourth measured velocity is shown in each direction, for clarity. At the most upstream shown plane (Figures 9a–c), the flow over the leading section of the ogive forebody (x'/D = 0.4) is measured, indicating that the local in-plane flow field is similar to that of the normal flow over a cylinder. There is a clear symmetry about the vertical axis, having the stagnation point at the central bottom (windward) surface, with vorticity layers growing along the side and into the leeward side. The two end states of the vortex layer are seeds of the forebody vortices. As the flow rolls over the forebody and into these vortices, towards the end of the forebody (x'/D = 1.8, Figures 9d–f), the windward side of the flow does not seem notably different, unless a closer look in taken into the stagnation point on the body, which becomes slightly deflected azimuthally under the asymmetric control (Figures 9d and f). Nearly perfect vertical symmetry of the leeward flow is preserved in the case of the control inner shell centered about θ= -2.5° (Figure 9e), indicating that bleed actuation enforces flow symmetry, as designed, aiming to suppress the net side force. It is noted that the details of the both CW and CCW vortex interaction with the surface are resolved in the measurements by the secondary vortical layers next to the surface of the opposing sign to the forebody vortex. In contrast to Figure 9e, the other two flow states indicate the evolving wake flow asymmetry in the other two controlled cases, having a signature initial deflection of the

CCW (Figure 9d) and CW (Figure 9f) vortex while continuing to evolve along the surface. If this plane were to be considered in isolation, the induced flow asymmetry would result in the positive (directed to the CW-vorticity side) in Figure 9d, and the opposite in Figure 9f. As it can be expected, further downstream flow evolution over the cylindrical body ($x'/D = 2.6$), seen in Figures 9g–j, only further amplifies this noted flow evolution. The flow control effecting the flow symmetry still maintains a reasonably symmetric flow field about the body (Figure 9h), while the asymmetric flow states show further deflection of one of the forebody vortices away from the surface. It is noted that, just as is the case at $x'/D = 1.8$, the CCW vortex in the control case shown in Figure 9g becomes deflected further away from the surface than its counter pair CW vortex in Figure 9j. As noted earlier, the lack of perfect antisymmetry between these two states is due to the naturally asymmetric flow field surrounding the body, which would evolve in the absence of flow control. Another interesting feature seen in Figures 9g and j is that displacement of one of the vortices couples to bending of the opposite vortex even further azimuthally along the cylinder, as both the CW vortex in Figure 9g and the CCW vortex in Figure 9j are drawn almost atop the cylinder at this cross-section of the flow. Clearly, such a joint action of the vortex pair only enhances the flow asymmetry and thereby its local contribution to the net unbalanced side force.

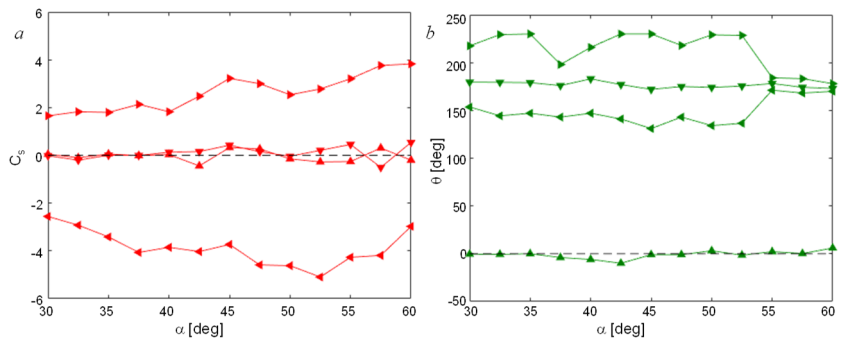

Figure 10. *Realized side force coefficients (a) and the corresponding control angles (b) over the full range of 30° ≤ α ≤ 60° for the control nominally centered about θ = 0° (▲), 180° (▼), 135° (◀), and 225° (▶), for U_o = 26 m/s.*

As a summary of the three possible flow realizations under the bleed flow control, Figure 10a shows the resulting side force coefficients attained for four different bleed inner shell orientations over the full range of the pitch angles 30° < α < 60° in increments of 2.5°. In addition, the inner shell orientations paired with each of the side forces are shown in Figure 10b. At each angle of attack α, the inner shell orientation is adjusted until the side force is maximized in either direction or until the force is nearly nulled. As discussed earlier, there are two azimuthal locations that can yield zero side force, the windward stagnation point and its opposing point on the leeward side. Therefore, there are two realizations of the zeroed side force, for the angles centered about $\theta = 0°$ and 180°, as seen in Figure 10b. The results in Figure 10a indicate that a significant suppression of the side force can be attained across the full range of the angles of attack with minimal adjustments of the nominal inner shell orientation, either about the windward stagnation point or on the vortex pair side (Figure 10b). The maximum controlled side force magnitude generally increases with the rise in the angle of attack (Figure 10a), where the corresponding control angles (Figure 10b) remain about the nominal values (approximately $\theta = 150°$ and 225°) up to the highest as, where these angles approach $\theta = 180°$ from below and above, respectively. It should be emphasized that the axisymmetric body at extreme angles of attack begins to approach a different class of flows, namely a finite cylinder (with a modified end) in the oncoming flow at $\alpha = 90°$, and as the model axis orientation changes from being aligned with the flow ($\alpha = 0°$) to being normal to the flow ($\alpha = 90°$), it is to be expected that the flow would also be transitioning from having a dominant vortex pair coupling to the wake to a modified Karman vortex street flow

over a finite cylinder with an end cap/ogive. Hence, it is to be expected that a flow control scheme designed to address this flow would have to be modified as the flow becomes dominated by a Karman vortex street. In addition, as noted above, there is a difference between the peak side force that can be attained with respect to the total force direction, as seen in Figure 10a, where the negative side force consistently dominates in magnitude, due to the natural preference of the flow to develop the net side force in that direction in the absence of flow control.

V. Upstream Alteration of the Forebody Vortex Pair

The final section of the present study examines the effects of bleed actuation on the forebody vortex pair over the forebody bleed interaction domain and downstream of the juncture to the main cylinder. As noted in Section III, the present PIV measurements are acquired within the axial domain $0.1 < x'/D < 3.4$ across 34 equally-spaced, axially-normal PIV measurement planes, while bleed actuation is applied within $0.25 < x'/D < 1.83$ over the forebody. A composite vortical field about the model is shown in Figure 11 for each of the three characteristic controlled flow evolutions: the resulting net positive ($\theta = 135°$, Figure 11a), zero ($\theta = 177°$, Figure 11b), and negative ($\theta = 225°$, Figure 11c) side force, where the net zero force is controlled on the vortex pair side. In this top view, a clear difference in the controlled vortex pair evolution past the forebody is noted. Initially, though, not much difference is observed during the vortex pair rollup about the forebody tip, regardless of the single-path bleed inner shell orientation. However, while the vortex pair evolution remains quite symmetric along the model axis in Figure 11b, their evolution becomes biased towards either side of the model in Figures 11a and c, where the CCW (Figure 11a) or CW (Figure 11c) vortex starts to deflect away from the surface, while the opposite vortex bends under it towards the model centerline. Clearly, not only the vortices but the whole wake, of which the vortices are integral part, becomes progressively asymmetric along the body in these two cases. Although not measured within the present study, previous research (Lee et al., 2023) clearly indicates that such global asymmetry of the wake continues to grow past the body and into the open wake, while the secondary vortex pair that forms along the cylindrical body downstream from the primary vortex pair deflection into the wake, lessens the flow asymmetry about the body surface. It is interesting that such a global flow evolution from the forebody tip to the body tail indicates that, along with the near-body asymmetrical evolution, the contribution to the net side force from the forebody flow is initially very small and then becomes significant and intensifies in the streamwise direction along the cylindrical body until becoming weakened past the formation of the secondary vortex pair along the cylinder.

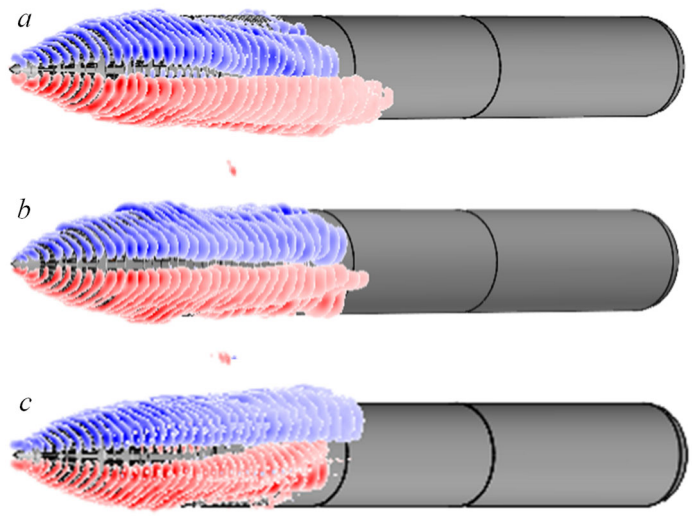

Figure 11. *A composite vortical flow reconstructed from the PIV-measured flow fields in twenty-five axial planes for the bleed control at $\theta = 135°$ (a), 177° (b), and 225° (c), for $\alpha = 45°$ and $U_o = 26$ m/s.*

Detailed characterization of the vortex pair trajectories for the three cases shown in Figure 11 is first done in terms of the extracted vortex trajectories. For that purpose, in each of the averaged flow

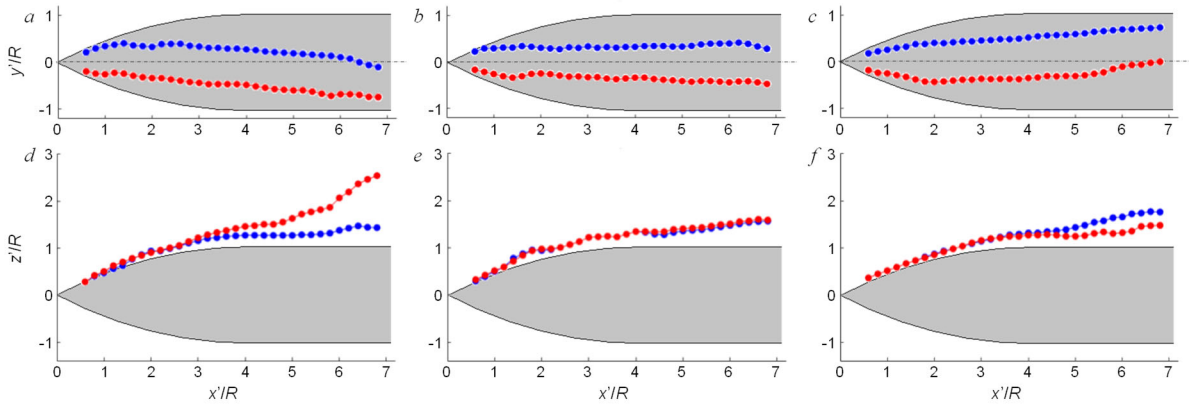

Figure 12. *Top (a – c) and side (d – f) views of the CW (●) and CCW (●) vortex trajectories for the bleed control at $\theta = 135°$ (a,d), 177° (b,e), and 225° (c,f), for $\alpha = 45°$ and $U_o = 26$ m/s.*

fields, closed contours of each of the vortices are extracted, followed by their center detection using the Γ_1 criterion. Lastly, such extracted trajectories are shown in Figure 12 in both the top (Figures 12a–c) and side (Figures 12d–f) views. The top views of the vortex trajectories are in accord with the vorticity evolution inferred from Figure 11, indicating a nearly parallel and symmetric trajectory of each vortex in the pair, a clear indication about the symmetry of the whole flow field about the body when the control inner shell is oriented at $\theta = 177°$ (Figure 12b). In addition, it is seen in Figure 12e that vortices become gradually displaced in unison away from the surface in the streamwise direction, maintaining their symmetry about the vertical central plane. Similarly, as already inferred from Figure 11, the extracted vortex trajectories for the positive (Figure 12a) and negative (Figure 12c) confirm the joint trajectory deflection to the side of the initial premature vortex lift off. This asymmetry is further emphasized in the corresponding side-view trajectories, particularly in the positive side force case (Figure 12d), where the sudden lift off of the CCW vortex begins about past $x'/D = 1.5$, and it is shed into the wake by the end of the measurement domain. It is also noted that as the CCW vortex is rapidly displaced, the CW displacement away from the surface is suppressed. Hence, both of these effects promote asymmetry in the flow. As noted in connection with Figures 9g and j, the displacement of the CW vortex in Figure 12f does not exactly mirror the opposite CCW vortex trajectory in Figure 12d, and the asymmetry in the flow progresses in a more gradual manner for this actuation case.

Finally, the vorticity flux of each vortex enables the vortex circulation estimate. Therefore, the evolution of each of three vortex pairs is shown in Figure 13 for the three characteristic bleed actuation configurations presented in Figure 11. Each plot also includes projections of the bleed port that are marked by dashed lines for reference. In common with the vortex pair trajectory in Figure 12, there is no significant change in the vortex pair circulation for all control configurations through the last axial bleed ports. While the circulation buildup is observed across the bleed ports in each of the configurations, past the bleed ports the circulation is reduced. In the configuration that leads to zero-force (Figure 13b) the circulation of the vortices not only remains balanced but it is also nearly invariant. In the configurations that leads to net side forces (Figures 13a and c), the initial drop in the circulation is followed by the asymmetric increase in circulation of the vortex that is displaced away from the surface, serving as an indicator of the resulting net side force on the model. That there is no significant change in the evolution of the vortex pair until the downstream end of the bleed ports even when the actuation is applied asymmetrically (CCW, Figure 13a, or CW, Figure 13c) implies that the effects of bleed interaction with the cross flow become pronounced only

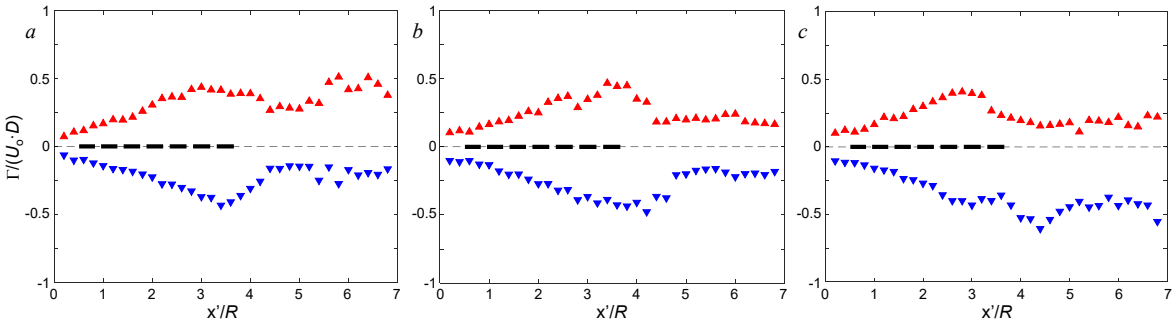

Figure 13. *Axial evolution of the CW (▲) and CCW (▲) vortex circulations for the bleed control at $\theta = 135°$ (a), 177° (b), and 225° (c), for $\alpha = 45°$ and $U_o = 26$ m/s. Dashed lines mark the axial projections of the bleed ports.*

downstream of the actuation domain. Since the single-path inner shell (cf. Figure 4d) drives both the inflow and outflow over the same surface segment, locally, it is anticipated that the inflow takes place predominantly over the upstream bleed ports, while the outflow that induces the interaction with the vortices, is mostly confined to the downstream end of the bleed section.

VI. Conclusions

The present experimental study builds on the initial investigations of Lee et al. (2023) that demonstrated the effectiveness of aerodynamic bleed actuation for controlling the side loads on axisymmetric bodies at high incidence. The motivation for the current work stems from the need to obviate the uncertainty associated with the magnitude and direction of side forces that are arbitrarily induced by geometric surface imperfections, as well documented in the literature. The present work seeks to demonstrate the efficacy of dynamically adjustable forebody bleed actuation mechanism that can effect desired side forces of variable magnitude and direction, and, specifically, can nullify arbitrary side forces in the absence of control.

In the present investigations, the forebody of the wind tunnel model of Lee et al. (2023) with prescribed arrays of azimuthal bleed ports (20% total porosity) was modified to house a miniature, computer-controlled rotary actuator to drive an inner conical shell to address azimuthal segments of the bleed ports for time-dependent, prescribed bleed configuration. Two shell configurations were investigated namely, single- or a dual-path shells with 90°-arc openings. The commanded azimuthal orientation of these shell openings underneath the outer shell yielded desired, azimuthal distributed arrays of bleed ports over the surface of the forebody.

The present investigations showed that the arbitrary side force effected by random surface imperfections can be nulled by proper orientation of the shell about the windward and leeward stagnation points. Furthermore, azimuthal changes of the shell position within up to ±15° about the null position were sufficient to vary prescribed side forces of desired sense and magnitude in either direction up to some maximum that increases with angle of attack. Furthermore, it was shown that the flow response to a step-like change in the shell orientation from one end state (maximum side force) to the opposite end state (minimum side force) is on the order of $4T_{conv}$ convective time scales. Time periodic rapid switch between the end states can be effected up to 6.6 Hz. Accompanying PIV measurements of the full flow field about the forebody and part of the cylinder (up to $x'/D < 3.4$), clearly link the resulting aerodynamic forces to the asymmetry of the flow field about the central vertical plane such that the net induced side force is normal direction of the side of the forebody vortex that remain closer to the surface. Therefore, both the evolution of the forebody vortex pair trajectories and their circulations, are indicative of the

resulting net side forces and moments where the bleed actuation is manifested by detachment of the affected forebody vortex away from the cylinder's surface while the opposite vortex in the absence of actuation remains close to the surface and bends toward the body axis. Replacing the single-path shell with a dual-path shell having the same arc opening leads to four azimuthal null positions of the prescribed side forces such that these forces can be varied in four azimuthal increments for finer aerodynamic control confirming that azimuthal bleed actuation can be effectively applied for aerodynamic control of axisymmetric platforms at high angles of incidence.

Acknowledgment

This work was supported by the Army Research Office, monitored by Dr. J. Edwards.

References

Allen, J. H. and Perkins, E. W., "Characteristics of Flow over Inclined Bodies of Revolution," NACA RM-A50L07, 1951.

Bauer, S. X. S. and Hemsch, M.J., "Alleviation of Sideforce on Tangent-Ogive Forebodies Using Passive Porosity," *Journal of Aircraft*, Vol 31, No 2, 1994, pp. 354-361.

Chapman, G.T., Keener, E.R., and Malcolm, G.N., "Asymmetric Aerodynamic Forces on Aircraft Forebodies at High Angles of Attack - Some Design Guides," AGARD Conference Proceedings AGARD-CP-199 (12), 1976.

Del Frate, J. H., and Saltzman, J. A., "In- Flight Flow Visualization Results From the X-29A Aircraft at High Angles of Attack", AIAA-92-4102, 1992.

DeSpirito, J., "CFD Aerodynamic Characterization of 155-mm Projectile at High Angles-of-Attack," *AIAA Paper* 2017-3397, 2017.

Ericsson, L.E. and Reding, J.P., "Alleviation of Vortex-Induced Asymmetric Loads," *Journal of Spacecraft and Rockets,* Vol. 17, No. 6, 1980, pp. 546-553.

Ericsson, L. E. and Reding, J. P., "Asymmetric Vortex Shedding from Bodies of Revolution," *Progress in Astronautics and Aeronautics, Tactical Missile Aerodynamics*, Vol. 104, 1986, pp. 243-296.

Fears, S. P., "Low-Speed Wind-Tunnel Investigation of a Porous Forebody and Nose Strakes for Yaw Control of a Multirole Fighter Aircraft," *NASA CR-4685*, 1995.

Hunt, B. L., 1982, "Asymmetric Vortex Forces and Wakes on Slender Bodies", AIAA-82-1336, 1982.

Keener, E. and Chapman, G., "Onset of Aerodynamic Side Forces at Zero Sideslip on Symmetric Forebodies at High Angles of Attack," *AIAA Paper 74-0770*, 1974.

Kumar, R., Viswanath, P. R., & Ramesh, O. N, "Nose Blowing for Side Force Control on Slender Cones at High Incidence," *Journal of Aircraft*, Vol. 45, No. 5, 2008, pp. 1156-1166.

Lambert, T.J., Vukasinovic, B., and Glezer, A., "A Six Degrees of Freedom Dynamic Wire-Driven Traverse," *Aerospace* Vol. 3: 11, 2016.

Lamont, P. J., "Pressures Around an Inclined Ogive Cylinder with Laminar, Transitional, or Turbulent Separation," *AIAA Journal*, Vol. 20, No. 11, 1982, pp. 1492-1499.

Lee, E., Huang, Y., Vukasinovic, B., and Glezer, A., "Controlled Aerodynamic Loads on a Slender Axisymmetric Body at High Incidence," *AIAA Paper* 2021-1943, 2021a.

Lee, E., Huang, Y., Vukasinovic, B., and Glezer, A., "Aerodynamic Flow Control of an Unstable Slender Cylindrical Body at High Incidence," *AIAA Paper* 2021-2610, 2021b.

Lee, E., Vukasinovic, B., and Glezer, A., “Controlled Loads on an Axisymmetric Platform at High Incidence using Forebody Aerodynamic Bleed,” *AIAA Paper* 2023-0432, 2023.

Leu, T.-S., Chang, J.-R. and Lu, P.-J., “Experimental Investigation of Side Force Control on Cone-Cylinder Slender Bodies with Flexible Micro Balloon Actuators,” *Exp. Ther. Fl. Sci.*, Vol. 29, No. 8, 2005, pp. 909-918.

Mahadevan, S., Rodriguez, J., and Kumar, K., “Effect of Controlled Imperfections on the Vortex Asymmetry of a Conical Body,” *AIAA J.*, Vol. 56, 2018, pp. 3460-3477.

Nelson, R. C., Pelletier, A., “The unsteady aerodynamics of slender wings and aircraft undergoing large amplitude maneuvers”, Progress in Aerospace Sciences, Volume 39, Issues 2–3,2003.

Porter, C., Seidel, J., Fagley, C., Farnsworth, J., McLaughlin, T., “Vortex Dynamics of a Tangent Ogive at a High Angle of Attack”, AIAA, 2012 -2953, 2012.

Porter, C., Fagley, C., Farnsworth, J., Seidel, J., and McLaughlin, T., "Closed-loop Flow Control of a Forebody at a High Incidence Angle" *AIAA journal* 52, no. 7(2014): 1430-1440.

Wang, Q., Cheng, K., Gu, Y., Li, Z., "Continuous control of asymmetric forebody vortices in a bi-stable state", *Physics of Fluids* 1 February 2018; 30 (2): 024102.

Thomson, K.D. and Morrison, D.F., “The Spacing, Position and Strength of Vortices in the Wake of Slender Cylindrical Bodies at Large Incidence,” *J. Fluid Mech*, Vol. 50, 1971, pp. 751-783.

Xueying D., Xuerui C., Yankui W., and Peiqing L., “Influence of Nose Perturbation on Behaviors of Asymmetric Vortices over Slender Body,” *AIAA Paper* 2002-4710, 2002.

Yanta, W. and Wardlaw, A., “Laser Doppler Velocimeter Measurements of Leeward Flowfields on Slender Bodies at Large Angle-of-Attack,” *AIAA Paper* 77-0668, 1977.

Yanta, W. and Wardlaw, A., “Flowfield about and Forces on Slender Bodies at High Angles of Attack,” *AIAA J.*, Vol. 19, No. 3, 1981, pp. 296-302.

Zilliac, G. G., Degani, D. and Tobak, M., “Asymmetric Vortices on a Slender Body of Revolution,” *AIAA J.*, Vol. 29, No. 5, 1991, pp. 667-675.